

Majorana bound states in nanowire-superconductor hybrid systems in periodic magnetic fields

Viktoriia Kornich,^{1,2} Maxim G. Vavilov,¹ Mark Friesen,¹ M. A. Eriksson,¹ and S. N. Coppersmith^{1,3}

¹*Department of Physics, University of Wisconsin-Madison, Madison, Wisconsin 53706, USA*

²*Kavli Institute of Nanoscience, Delft University of Technology, 2628 CJ Delft, The Netherlands*

³*School of Physics, The University of New South Wales, Sydney NSW 2052, Australia*

(Dated: November 18, 2019)

We study how the shape of a periodic magnetic field affects the presence of Majorana bound states (MBS) in a nanowire-superconductor system. Motivated by the field configurations that can be produced by an array of nanomagnets, we consider spiral fields with an elliptic cross-section and fields with two sinusoidal components. We show that MBS are robust to imperfect helical magnetic fields. In particular, if the amplitude of one component is tuned to the value determined by the superconducting order parameter in the wire, the MBS can exist even if the second component has a much smaller amplitude. We also explore the effect of the chemical potential on the phase diagram. Our analysis is both numerical and analytical, with good agreement between the two methods.

I. INTRODUCTION

Majorana bound states (MBS) have been of great interest for quantum computing over the past two decades due to their non-Abelian statistics and robustness against local perturbations^{1,2}. Different models for creation of MBS have been suggested and studied^{1–30}. One of the models, which has attracted much attention because of its potential experimental feasibility, is a nanowire-superconductor hybrid system^{11,12}. It is constructed from a nanowire with strong spin-orbit interactions in a uniform magnetic field on a superconducting substrate, which induces superconductivity in the nanowire due to the proximity effect. The Hamiltonian for the semi-conducting part of this device, i.e. the nanowire with spin orbit interaction and a uniform magnetic field, is related by a unitary transformation to a Hamiltonian for a nanowire with a helical magnetic field and no spin orbit interaction³¹. The presence of MBS in nanowires and carbon nanotubes with helical magnetic fields was studied in Refs. 16 and 32. It was also suggested to create a similar setup with a helical-shaped effective magnetic field via magnetic atoms on top of a superconductor^{25,33–38}. Non-uniform magnetic fields, created by an array of nanomagnets, can be used to create MBS in a nanowire-superconductor hybrid system^{17,18}. The formation and braiding of MBS via a nanomagnet pattern on a 2D substrate was discussed in Refs. 39 and 40. There are other suggestions for devices with various magnetic field shapes and origins which may host MBS, e.g., Refs. 41–43.

Recent work in Ref. 44 presented detailed modelling of the magnetic field due to an array of nanomagnets acting on a nanowire in a Si heterostructure. As Si is widely used in modern technology, and therefore a material convenient for potential applications, it can be useful for an experimental realization of MBS to study whether certain Si structures can host MBS. Here, we consider a Si nanowire with superconductivity induced by the proximity effect and with nearby nanomagnets that can be made out of Co or SmCo⁴⁴.

In this work, we investigate when a topological superconducting phase in lithographically defined Si nanowires exists. Using parameters that are reasonable for lithographically defined silicon nanowires and magnets (see Sec. II A), we con-

sider 25-nm wide wires with a superconducting gap $\sim 5 \mu\text{eV}$ and with the magnetic field produced by nanomagnets with strength about 100 mT, see Fig. 1. These conditions are sufficient for a perfect helical magnetic field to produce the topologically non-trivial superconducting phase that supports an MBS with localization length of about $1 \mu\text{m}$ ^{16,31,32}. Since an ideal helix is difficult to achieve using micromagnets, we study how different shapes of the magnetic field would affect the presence of an MBS in a Si-based setup. In particular, we consider a spiral magnetic field with an elliptic cross section. For both ideal and non-ideal helical fields, a partial gap opens in the presence of a magnetic field. However in the non-ideal case, a second gap opens that is proportional to the difference between the major and minor axes of the spiral⁴⁴. If the chemical potential is tuned such that it is inside both gaps, the superconductivity and the MBS are both suppressed.

We investigate the phase boundary of the topological superconducting phase as a function of the major and minor axes of the spiral elliptic magnetic field. The boundary between topological and non-topological phases is marked by the vanishing of the superconducting gap around the chemical potential. In the non-topological phase, there are no states below the gap, while in the topological phase two additional states, the MBS localized at the wire edges, develop. The localization length of the MBS decreases quickly as the superconducting gap recovers away from the phase boundary. Thus, we use the existence of two states with eigenenergies below the superconducting gap, together with their localization near edges, as a criterion for the topological phase. We demonstrate that the eigenenergies of the topological state are exponentially suppressed for long enough wires, yielding effective zero-energy modes that are associated with the topological superconducting phase.

MBS develop in the presence of a perfect helical magnetic field when the field magnitude exceeds a threshold value equal to the superconducting order parameter in the wire^{16,31,32}. A small deformation of the perfect helix is not expected to immediately destroy the MBS. Our analysis demonstrates the robustness of the MBS to relatively strong deformation of the helical field. As we demonstrate below, when one amplitude of the oscillating magnetic field is tuned so that it is about twice the value of the superconducting order parameter in the

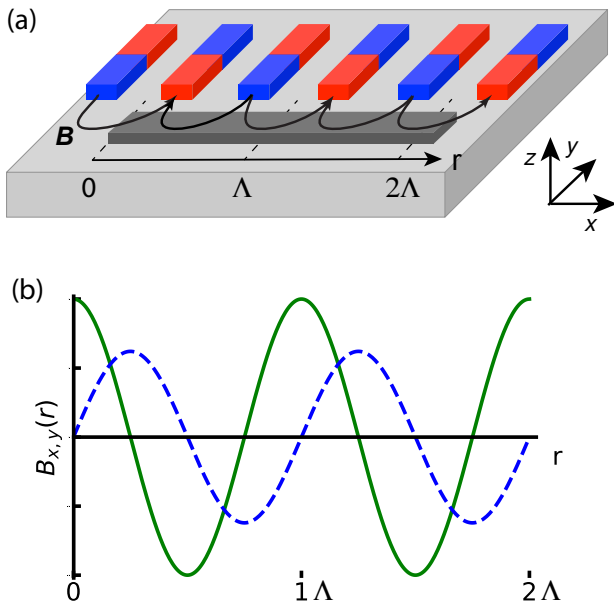


FIG. 1. (a) A schematic representation of the system geometry. Here, the nanowire (orange cylinder) is in proximity with a superconductor (grey rectangle). Nanomagnets with alternating magnetization are arranged nearby (blue-red rectangles), in the same plane as the wire. Alternatively, the nanomagnets can be positioned higher than the nanowire, which could improve the shape of the magnetic field for our purposes⁴⁴. (b) Components of the spiral magnetic field, $B_x = B_{x0} \cos(2\pi r/\Lambda)$ (solid line) and $B_y = B_{y0} \sin(2\pi r/\Lambda)$ (dashed line) in the nanowire, with period Λ , as a function of position along the wire, r . For an ideal helical field, we have $B_{y0} = B_{x0}$. Here, we show the case of an elliptic helical field, with $B_{y0} = 0.62B_{x0}$.

wire, the MBS develop even when the second component of the field is much smaller; thus, when the magnitude of one of the field components is tuned appropriately, the MBS can survive even very strong ellipticity of the helical magnetic field. We also show that the analytic solution of a continuum model with a linearized energy dispersion provides a good guide for understanding the numerical results obtained for finite, discretized wires.

The paper is organized as follows. In Sec. II we discuss the experimental constraints on the model parameters for an example system of a nanowire in which the superconductivity is induced by the proximity effect and magnets are patterned lithographically. We then present the Hamiltonian that we analyze in the succeeding sections, II B and II C. We present an analytical derivation of the MBS wave function and the spectrum for a spiral magnetic field with an elliptic cross-section in Sec. III. Sec. IV A presents numerical results for the phase diagrams for the different shapes of the magnetic field. Our conclusions follow in Sec. V.

II. MODEL OF SUPERCONDUCTING NANOWIRE IN PERIODIC MAGNETIC FIELD

A. Estimations of experimental parameters

While the focus of this work is theoretical, it is important to note that the physical regimes are realistic. An example physical system is a silicon nanowire, whose width we estimate below, with superconductivity induced by the proximity effect, either from metals⁴⁵ or from the superconductivity in a nearby, very highly doped semiconductor region⁴⁶. Lithographically defined Co and SmCo nanomagnets⁴⁴ deposited nearby give rise to appropriate helical field variations, as shown in Fig. 1.

We now estimate the transverse width of the nanowire and its associated Fermi wavelength. Because the experimental parameters of interest (e.g., the threshold density) are better characterized in two-dimensional (2D) systems than in wires, we will refer to 2D experiments as a starting point. The six-fold valley degeneracy of the conduction band in bulk silicon is lifted by tensile strain or by narrow confinement, leaving just two low-energy valleys to form a quantum device⁴⁷. The remaining degeneracy is lifted by wavefunction overlap with sharp interfaces, with a valley energy splitting of δ_v . Assuming a parabolic dispersion relation for the two-dimensional electron gas (2DEG), the lower (l) and upper (u) valley band energies are given by $\varepsilon_l(\mathbf{p}) = p^2/2m$ and $\varepsilon_u(\mathbf{p}) = p^2/2m + \delta_v$, where \mathbf{p} is a two-dimensional quasi-momentum and $m = 1.73 \times 10^{-31}$ kg is the transverse effective electron mass. Here, we choose $\delta_v \lesssim 100 \mu\text{eV}$ as the valley splitting of a typical 2DEG⁴⁸, although there is some evidence of larger valley splittings in wire geometries, depending on the confinement⁴⁹.

The Fermi energy E_F should be large enough to allow the nanowire to conduct, where E_F is measured from the bottom of the lower valley in the 2DEG dispersion. Normally the threshold electron density needed for a 2DEG to conduct is smaller than for a wire, since any disorder disrupts the current flow in the one-dimensional case. For a nanowire, we therefore assume an electron density n_e for which the Fermi energy is higher than the maximum value of the disorder potential. The Fermi energy and the electron density are then related by

$$n_e = \frac{2m(2E_F - \delta_v)}{2\pi\hbar^2}, \quad (1)$$

assuming spin degeneracy.

To determine the size of the nanowire, we assume a harmonic confinement potential in the transverse direction with a root-mean-square width of the wavefunction, σ_w , corresponding to an energy level splitting of

$$\hbar\omega_0 = \frac{\hbar^2}{m\sigma_w^2}. \quad (2)$$

Since the valley degree of freedom represents an unwanted quantum variable, we can suppress the filling of the upper valley band by adjusting the ground-state energy $\hbar\omega_0/2$ such that it lies between the highest filled state and the lowest unfilled

state:

$$E_F - \delta_v < \frac{\hbar\omega_0}{2} < E_F. \quad (3)$$

To satisfy this constraint, we adopt $\sigma_w = 25$ nm, yielding an upper limit of $n_e = 5.9 \times 10^{10} \text{cm}^{-2}$ for the electron density, which as desired is significantly higher than the threshold electron density of a conducting 2DEG, $n_{e,\text{th}} = 2 \times 10^{10} \text{cm}^{-2}$, as reported in Ref. 50 for a 100 nm deep Si/SiGe quantum well.

The chemical potential in the wire is counted from the bottom of the one-dimensional conduction channel, such that

$$\mu = E_F - \frac{\hbar^2}{2m\sigma_w^2},$$

with a corresponding Fermi wavevector of $k_F = \sqrt{2m\mu/\hbar^2}$. Here we choose $\mu \simeq 50 \mu\text{eV}$, so that the occupation of the higher valley is well suppressed.

Finally, we estimate the values of the magnetic field B and the proximity-induced superconducting gap in the nanowire Δ that support an MBS. For a perfectly helical magnetic field, the presence of an MBS requires fields with $g\mu_B B > \sqrt{\Delta^2 + \delta\mu^2}$ ^{16,17}, where the Landé g -factor $g \approx 2$ for Si, μ_B is the Bohr magneton, and $\delta\mu = \mu - \hbar^2 Q^2/2m$ is the detuning of the chemical potential away from the center of the energy gap ($\hbar^2 Q^2/2m$), caused by a magnetic superlattice with period Λ (see Fig. 1) and wavevector $Q = 2\pi/\Lambda$. (Henceforth, we adopt energy units for B by absorbing $g\mu_B$ into its definition.) Because it is difficult to achieve Zeeman splittings in excess of $20 \mu\text{eV}$ using nanomagnets, we take $\Delta = 5 \mu\text{eV}$ here. This choice also satisfies the condition $\mu \gg \Delta$, which is necessary for achieving a proximitized superconducting gap in the wire.

B. Magnetic superlattice

In the following two sections, we present the Hamiltonian studied in this work. First, we introduce a periodic magnetic field in the absence of superconductivity. In Sec. II C, we then include the effects of superconductivity.

We consider the Hamiltonian for a single electron in the wire with parabolic energy dispersion in the presence of a magnetic field $\mathbf{B}(r) = \{B_x(r), B_y(r), B_z(r)\}$ that oscillates periodically as a function of the coordinate r along the wire:

$$H_Z = \varepsilon_l(\mathbf{p}) + \mathbf{B}(r) \cdot \boldsymbol{\sigma} - \mu, \quad (4)$$

where $\boldsymbol{\sigma} = \{\sigma_x, \sigma_y, \sigma_z\}$ are Pauli matrices.

The actual magnetic field configuration produced by nanomagnets is complex. Field configurations produced by arrays of bar-shaped nanomagnets as well as electron spectra are calculated in Ref. 44. It was also shown that a special configuration of magnetic fields may improve conditions for the MBS to develop. However, the goal of this paper is to investigate how deviations from the perfect helical magnetic field may affect the topologically non-trivial superconducting phase. For

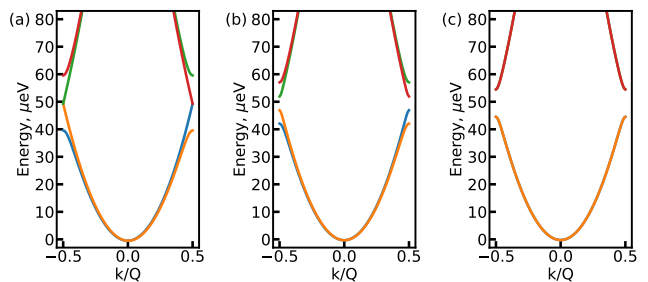


FIG. 2. The band structure (energy versus normalized wavevector k/Q) of an electron in the presence of the periodic, helical magnetic field, defined in Eq. (5), with period $\Lambda = 2\pi/Q = 200$ nm. (a) An ideal helical magnetic field $B_{x0} = B_{y0} = 10 \mu\text{eV}$. (b) An elliptical magnetic field $B_{x0} = 10 \mu\text{eV}$ and $B_{y0} = 5 \mu\text{eV}$. (c) A non-chiral magnetic field $B_{x0} = 10 \mu\text{eV}$ and $B_{y0} = 0$. States with the two spin chiralities with energies below the gap are denoted in orange and blue, while states with the two spin chiralities with energies above the gap are denoted in red and green. For the ideal helical field (a), a gap opens for one spin chirality but not the other, so there are states in at least one band for all values of the chemical potential. When the field is non-chiral (c), the energy dispersions of the different spin helicities are the same, and there is no chemical potential for which one band is gapped and the other is not. (The blue and green curves are not visible on the plot because they are identical to the orange and red curves.) When the field is chiral but not an ideal helix (b), the gaps of the two helicities are different, and there are values of the chemical potential that are in the gap for one chirality but not the other.

this purpose, we use a helical magnetic field with elliptical helical cross-section:

$$B_x = B_{x0} \cos Qr, \quad B_y = B_{y0} \sin Qr, \quad B_z = 0, \quad (5)$$

where $Q = 2\pi/\Lambda$ is the vector of the reciprocal 1D Bravais lattice of the magnetic superlattice with period Λ and $B_{x0}, B_{y0} \geq 0$. We note, that due to the absence of the spin-orbit interaction in this system, the direction of the wire and magnetic field orientation are completely decoupled. For example, the system properties remain the same regardless of the choice of the magnetic components x, y relative to the wire direction.

For the magnetic field given by Eq. 5, the matrix elements of the magnetic periodic potential are non-zero only for two reciprocal vectors $\pm Q$:

$$W_{\pm Q} = \frac{1}{2} \begin{pmatrix} 0 & B_{x0} \pm B_{y0} \\ B_{x0} \mp B_{y0} & 0 \end{pmatrix}. \quad (6)$$

The spectral equation for electron states in the magnetic superlattice has the form

$$\left(\frac{\hbar^2(k - nQ)^2}{2m} - \mathcal{E}(k) \right) c_{k-nQ} + \sum_{\pm} W_{\pm Q} c_{k-(n\pm 1)Q} = 0, \quad (7)$$

where $n = 0, \pm 1, \pm 2, \dots$ and the spinor coefficients c_{k-nQ} define the electron wave function $\psi_k(r) = \sum_n c_{k-nQ} \exp(i(k - nQ)r)$ ^{44,51}.

Using Eq. (7), we can determine that there are energy gaps at the edges of the Brillouin zone with magnitudes $|B_{x0} \pm B_{y0}|$. For an ideal helical field with $B_{x0} = B_{y0}$, one branch has a large gap $B_{x0} + B_{y0}$, while the other branch is gapless. However, when $B_{x0} \neq B_{y0}$, both gaps are nonzero, and there are no states within the energy window $|B_{x0} - B_{y0}|$ around $\epsilon = \hbar^2 Q^2 / 8m$.

We solve Eq. (7) for the magnetic field period $\Lambda = 200$ nm in Si nanowire. The energy bands are shown in Fig. 2(a) for $B_{x0} = B_{y0} = 10$ μeV , in Fig. 2(b) for $B_{x0} = 2B_{y0} = 10$ μeV , and in Fig. 2(c) for $B_{x0} = 10$ μeV , $B_{y0} = 0$. For the last case, the magnetic field is non-chiral, the two spin helicities have identical band structures, and no topologically nontrivial phase is supported.

Using parameters from Subsec. II A, we find that $\Lambda = 200$ nm is an acceptable scale for nanofabrication and at the same time allows the lifting of the valley degeneracy of the conducting channel in the wire. Indeed, the magnetic structure would require fabrication of pairs of 50 nm wide nanomagnets with opposite magnetizations, see Fig. 1.

C. Hamiltonian for superconducting wire

We now add to the Hamiltonian the superconductivity terms that pair electrons with energies above the chemical potential with holes below the chemical potential. This coupling is conveniently represented by the electron creation and annihilation operators in the Nambu space defined by the vector $\Psi = \{\psi_\uparrow, \psi_\downarrow, \psi_\uparrow^\dagger, \psi_\downarrow^\dagger\}^T$. The Hamiltonian of the system can be written as

$$\mathcal{H} = \int \Psi^\dagger(r) H \Psi(r) dr, \quad (8a)$$

where the Hamiltonian matrix in the Nambu space is

$$H = \begin{pmatrix} H_Z & i\Delta\sigma_y \\ -i\Delta\sigma_y & -H_Z^* \end{pmatrix}, \quad (8b)$$

where r is the position along the wire, Δ is the superconducting gap, and the single-electron Hamiltonian H_Z is given by Eq. (4). This Hamiltonian has eigenvectors that are solutions to the Bogolyubov-De Gennes (BdG) equation⁵²

$$H\Psi = E\Psi. \quad (9)$$

Below we will investigate the eigenenergies and eigenstates of this Hamiltonian by finding solutions of the BdG equation numerically.

The electron wavefunctions can be rewritten in the Majorana basis instead of the Nambu basis by introducing a unitary transformation of the vector Ψ , where the transformation matrix is given by

$$\Phi = U_M \Psi, \quad U_M = \frac{1}{\sqrt{2}} \begin{pmatrix} 1 & 0 & 1 & 0 \\ 0 & 1 & 0 & 1 \\ i & 0 & -i & 0 \\ 0 & i & 0 & -i \end{pmatrix}. \quad (10)$$

The MBS in this basis is represented by a real function with eigenenergy $E_0 \rightarrow 0$.

III. ANALYTICAL CHARACTERIZATION OF THE PHASE DIAGRAM

To provide analytic insight into when a magnetic field that does not have an ideal helical form induces MBS, we generalize the procedure described in Ref. 53 to apply to the case of a field with an elliptical cross section. We consider perfect matching between the Fermi momentum of 1D electrons in the wire and the periodicity of the magnetic superlattice by setting the chemical potential $\mu = \hbar^2 Q^2 / 8m$. We choose $B_{x0} > 0$ and $B_{y0} > 0$; this restriction is inessential because different signs of these components correspond to different chiralities of the magnetic field. The continuum and long-length limits examined here are expected to be applicable when the period of the magnetic field oscillations is much less than the length of the wire and when $B_{x0}, B_{y0}, \Delta \ll \mu$.

We represent the electron wave functions as a superposition of left- and right-movers

$$\psi_\sigma = R_\sigma e^{iQr/2} + L_\sigma e^{-iQr/2}, \quad (11)$$

where $\sigma = \{\uparrow, \downarrow\}$, and we linearize the energy dispersion in the kinetic energy term:

$$H_{\text{kin}} = -i\hbar v_F (R_\uparrow^\dagger \partial_r R_\uparrow - L_\uparrow^\dagger \partial_r L_\uparrow + R_\downarrow^\dagger \partial_r R_\downarrow - L_\downarrow^\dagger \partial_r L_\downarrow), \quad (12)$$

where the Fermi velocity is $v_F = \hbar Q / 2m$. The hole part of the Hamiltonian can be obtained from the anticommutation relations of the fermion operators and we do not explicitly show it here. We neglect all fast-oscillating terms, assuming that the localization length of the R and L functions is much larger than $2\pi/Q$. Later we show that this condition indeed holds for our results. The Zeeman term due to the magnetic field is

$$H_{\text{mag}} = \frac{1}{2} [(B_{x0} - B_{y0})(R_\uparrow^\dagger L_\downarrow + L_\downarrow^\dagger R_\uparrow) + (B_{x0} + B_{y0})(L_\uparrow^\dagger R_\downarrow + R_\downarrow^\dagger L_\uparrow)], \quad (13)$$

and the superconductivity term

$$H_{\text{sc}} = \Delta (R_\downarrow L_\uparrow + L_\downarrow R_\uparrow - R_\uparrow L_\downarrow - L_\uparrow R_\downarrow + H.c.). \quad (14)$$

The Hamiltonian can be decoupled into two non-interacting subspaces $\chi_- = \{R_\uparrow, L_\downarrow, R_\uparrow^\dagger, L_\downarrow^\dagger\}^T$ and $\chi_+ = \{L_\uparrow, R_\downarrow, L_\uparrow^\dagger, R_\downarrow^\dagger\}^T$. In these subspaces, the Hamiltonian has the form

$$H_\pm = \pm i\hbar v_F \partial_r \sigma_z - \delta\mu \tau_z + B_\pm \sigma_x \tau_z - \Delta \sigma_y \tau_y, \quad (15)$$

where $B_\pm = (B_{x0} \pm B_{y0})/2$ and $\delta\mu = \mu - \hbar^2 Q^2 / 8m$ is the mismatch between the chemical potential and the center of energy gap of electron bands of the magnetic superlattice. The energies of quasiparticle excitations of H_θ with $\theta = \pm$ for perfect matching of the chemical potential, $\delta\mu = 0$, are given by

$$E_\theta^\pm = \sqrt{\hbar^2 v_F^2 \delta k^2 + [B_\theta \pm \Delta]^2}, \quad (16)$$

where $\delta k = k \pm Q/2$ denotes momenta counted from Fermi points $\pm Q/2$ and we consider only non-negative energies. We

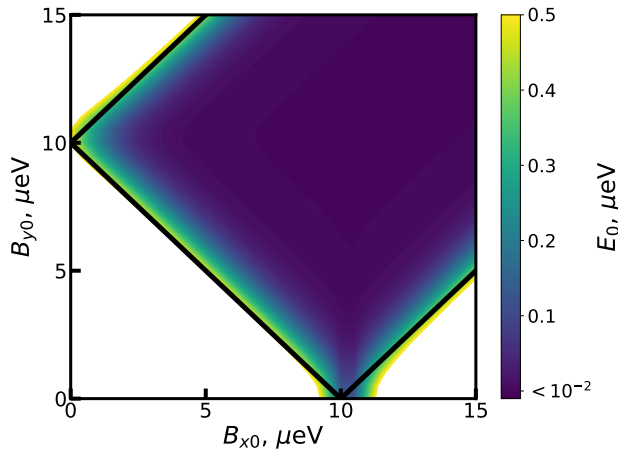


FIG. 3. Contour plot of E_0 , the energy of the state of lowest positive energy in the system, versus the magnetic field amplitudes B_{x0} and B_{y0} . Parameter values used are: superconducting order parameter $\Delta = 5 \mu\text{eV}$, magnetic field wavevector $Q = 2\pi/\Lambda$, $\Lambda = 200 \text{ nm}$, chemical potential $\mu = \hbar^2 Q^2 / 8m = 49.6 \mu\text{eV}$, and wire length $L = 20 \mu$. The uncolored region where $E_0 > 0.5 \mu\text{eV}$ corresponds to the gapped non-topological superconducting phase, the dark purple color denotes the region in which $E_0 < 10^{-2} \mu\text{eV}$, and the crossover region over which the zero energy state develops in this wire with finite length is evident in the transitions between colors in the color plot for the region of $E_0 < 0.5 \mu\text{eV}$. The solid straight lines show the analytical predictions for the phase boundary given by Eq. (21).

note that the two subspaces, $\theta = \pm$, describe two chiralities of electrons in the spiral magnetic field. Without the proximity effect, $\Delta = 0$, Eqs. (III) correspond to two branches with a smaller and larger magnetic gaps at the boundary of the Brillouin zone of the magnetic superlattice, see Subsec. II B and Fig. 2.

We observe that the excitation energy vanishes for $\delta k = 0$ when

$$\text{either } B_+ = \Delta \text{ or } B_- = \Delta. \quad (17)$$

These lines, which define the boundaries between topologically trivial and non-trivial superconducting phases in an infinitely long wire, are shown as solid straight lines in Fig. 3. Our next step is to demonstrate that the internal region in the phase diagram indeed supports the MBS.

Away from the lines defined by Eq. (17), there is no zero-energy eigenstate for real δk . However, the purely imaginary values of

$$\delta k_{\alpha,\theta}^{\pm} = \pm i \frac{\alpha B_{\theta} + \Delta}{\hbar v_F} \quad (18)$$

might describe zero-energy solutions that exponentially decrease or grow along the nanowire. The \pm sign in Eq. (18) defines the solutions that decrease or increase as a function of coordinate r along the wire and would correspond to two states localized at each of the ends of the nanowire, and $\alpha = \pm$

identifies the sign choice in Eq. (16). Here we focus on the solution that is localized near $r = 0$. In this case, we identify only one pair of $\delta_{\alpha,\theta}^{\pm}$ and $\delta_{\alpha,\theta}^{\pm}$ that satisfy the boundary condition $\Psi(r = 0) = 0$.

The general solution can be written as a linear combination of eight terms

$$\chi(r) = \sum_{\theta=\pm} \sum_{\alpha=\pm} \sum_{\sigma=\pm} \beta_{\alpha,\theta}^{\sigma} c_{\alpha,\theta}^{\sigma} \exp(ir\delta k_{\alpha,\theta}^{\sigma}) \quad (19)$$

of four linearly independent 4-component vectors

$$\begin{aligned} c_{-,-}^{+} = c_{-,+}^{-} &= \begin{pmatrix} 1 \\ i \\ 1 \\ -i \end{pmatrix}, & c_{+,-}^{+} = c_{+,+}^{-} &= \begin{pmatrix} 1 \\ -i \\ -1 \\ -i \end{pmatrix}, \\ c_{-,-}^{-} = c_{-,+}^{+} &= \begin{pmatrix} 1 \\ -i \\ 1 \\ i \end{pmatrix}, & c_{+,-}^{-} = c_{+,+}^{+} &= \begin{pmatrix} 1 \\ i \\ -1 \\ i \end{pmatrix}. \end{aligned} \quad (20)$$

The proper solution (19) vanishes at $r = 0$, so it must contain a pair of terms formed by one of the vectors of Eq. (20) and multiplied by the exponential functions $\exp(ir\delta k_{\alpha,\theta}^{\sigma})$ with different top index σ in $\delta k_{\alpha,\theta}^{\sigma}$. At the same time, each term in the pair must decrease as a function of r , i.e. $\text{Im}\{\delta k_{\alpha,\theta}^{\sigma}\} > 0$. We find that the first pair, $c_{-,-}^{+} = c_{-,+}^{-}$, satisfies these conditions, provided that

$$B_{x0} < 2\Delta + B_{y0}, \quad B_{x0} + B_{y0} > 2\Delta. \quad (21a)$$

However, addition requirement to the above inequalities is

$$B_{y0} < 2\Delta + B_{x0}. \quad (21b)$$

Otherwise, another solution with zero energy develops near $r = 0$, formed by the pair $c_{+,-}^{-} = c_{+,+}^{+}$ in Eq. (20). Overall, a non-degenerate solution of Eq. (15) with eigenenergy $E = 0$ and localized near $r = 0$ can exist within the rectangular region shown by bold solid lines in Fig. 3. Since the energy gap vanishes on these lines, we identify the region inside as the topologically non-trivial superconducting phase that supports the MBS. The outside region is the topologically trivial superconducting phase.

We comment on the localization length of the MBS. The length is determined by $\max\{1/|\delta k_{\alpha,\theta}^{\sigma}|\}$. The localization length diverges near the phase boundaries, but then saturates to $\hbar v_F / \Delta$ in the center of the topological superconducting phase at $B_{x0} = B_{y0}$. The predictions yielded by this continuum theory for the dependence of the localization length on model parameters will be compared with numerical results in the next section.

IV. PHASE DIAGRAM: NUMERICAL RESULTS

A. Discretized Hamiltonian

We now show the results of numerical calculations in which the approximations that enable the analytical calculations in

Sec. III are not made, obtaining results similar to those of the analytic model, as shown in Fig. 3. We now consider a finite-length wire. We calculate the eigenvalues and eigenstates of a discretized version of Eq. (8a) to determine the energy gap and identify the MBS. We rewrite the Hamiltonian represent-

ing the second derivative as a finite difference of the wave function $\Psi_n = \Psi(n\delta r)$ for a set of n points separated by a discretization distance δr along the wire; the total number of sites along the wire is $N = L/\delta r$. The full Hamiltonian is given by the $4N \times 4N$ matrix

$$\tilde{H} = \begin{pmatrix} & & \dots & & & & \\ & \hat{\mathcal{T}} & \hat{\mathcal{K}}_{n-1} & \hat{\mathcal{T}} & \hat{0} & \hat{0} & \\ \dots & \hat{0} & \hat{\mathcal{T}} & \hat{\mathcal{K}}_n & \hat{\mathcal{T}} & \hat{0} & \dots \\ & \hat{0} & \hat{0} & \hat{\mathcal{T}} & \hat{\mathcal{K}}_{n+1} & \hat{\mathcal{T}} & \\ & & & \dots & & & \end{pmatrix}, \quad (22)$$

where the diagonal blocks are

$$\hat{\mathcal{K}}_n = \begin{pmatrix} 2\tilde{T} - \mu + B_z^n & B_x^n - iB_y^n & 0 & \Delta \\ B_x^n + iB_y^n & 2\tilde{T} - \mu - B_z^n & -\Delta & 0 \\ 0 & -\Delta & -2\tilde{T} + \mu - B_z^n & -B_x^n - iB_y^n \\ \Delta & 0 & -B_x^n + iB_y^n & -2\tilde{T} + \mu + B_z^n \end{pmatrix}, \quad (23)$$

and the off-diagonal blocks are

$$\hat{\mathcal{T}} = \begin{pmatrix} -\tilde{T} & 0 & 0 & 0 \\ 0 & -\tilde{T} & 0 & 0 \\ 0 & 0 & \tilde{T} & 0 \\ 0 & 0 & 0 & \tilde{T} \end{pmatrix}. \quad (24)$$

The \tilde{T} terms are given by

$$\tilde{T} = \frac{\hbar^2}{2m\delta r^2} \quad (25)$$

and originate from the discretized kinetic energy

$$-\frac{\hbar^2}{2m} \frac{\partial^2 \Psi(r)}{\partial r^2} \rightarrow -\tilde{T} (\Psi_{n+1} - 2\Psi_n + \Psi_{n-1}). \quad (26)$$

The $B_{x,y,z}^n$ terms in Eq. (23) are components of the magnetic field $\mathbf{B}^n = \mathbf{B}(n\delta r)$ at site n . To be specific, we assume that the wire length L is a multiple of the magnetic period Λ . We implement the boundary conditions $\Psi(r=0) = \Psi(r=L) = 0$.

We diagonalize the discretized Hamiltonian and obtain the energy eigenvalues and eigenstates. The MBS, if present in the superconducting nanowire, is a non-degenerate state with energy in the middle of the superconducting gap that is zero in the limit of an infinite length wire and that is spatially localized at the ends of the nanowire. We use these conditions to build phase diagrams for our setup for different amplitudes of the magnetic field components. The eigenstates of the discretized Hamiltonian Eq. (22) are $4N$ vectors, where 4 elements in each of N blocks represent the four components of the electron wavefunction in the Nambu space.

We discuss the precise criteria for how we define zero energy and the gap energy in the numerical calculation for a finite system and the definition of the localization length in the following subsections of this section.

B. Energy gap and zero-energy excitations

Using the numerical method described above, we analyze the low energy eigenstates of the Hamiltonian Eq. (8a). For the results shown, the discretization length used in the numerical calculations is $\delta r = 20$ nm unless stated otherwise. This value of δr satisfies $\delta r \ll \Lambda$ and $\delta r \ll \hbar v_F/\Delta$, and we have checked that changing the value of δr does not change the numerical results significantly.

To identify the phase transition and the development of the MBS, it is sufficient to focus only on the behavior of the lowest energy excitations. To illustrate how MBS are manifest in the numerical results, we compare the lowest energy excitations for the ideal helical field with $B_{x0} = B_{y0}$ (where it is known that MBS are supported⁵³) to the lowest energy excitations when one of the field components is zero (when there is no field chirality and the phase is topologically trivial for all magnitudes of the nonzero component).

To explore the phase diagram in $B_{x0} - B_{y0}$ plane, we construct a color contour plot for E_0 for the wire of length $L = 20 \mu\text{m}$, shown in Fig. 3. In the uncolored regions of the plot, the lowest energy E_0 is above $0.1\Delta = 0.5 \mu\text{eV}$, which we identify as the gapped non-topological superconducting phase. In wires of finite length, the zero energy state develops over finite crossover region shown as transition colors when $E_0 < 0.5 \mu\text{eV}$, where E_0 quickly drops below $10^{-2} \mu\text{eV}$. This region can be identified as the topological superconducting phase with a superconducting gap in the density of states and a low-energy state inside the gap, corresponding to the MBS. We note that the crossover region is well described by the analytical expressions for the phase boundary evaluated in the previous section, see solid thick lines in Fig. 3 and Eqs. (17).

To illustrate the actual dependence of lower energies on the magnetic field, we show the two lowest two energies $E_{0,1}$ as function of the magnetic field strength $B_{x0} = B_{y0} = B_0$

in Fig. 4(a), this field configuration corresponds to a perfect helix studied earlier^{31,32,53}. When $B_0 = 0$, the values of both energies are just above the superconducting gap Δ . As B_0 is increased from zero, the effective superconducting gap $|B_0 - \Delta|$ as well as all three eigenenergies decrease. As B_0 is increased beyond Δ , the lowest energy E_0 continues to decrease monotonically towards zero, while the energy of the higher eigenstate goes through its minimum at $B_0 \simeq \Delta$ and then increases until it reaches an asymptotic value equal to the superconducting gap Δ . Here, there is a topologically nontrivial phase when $B_{x0} = B_{y0} > 2\Delta$, and the lowest energy E_0 approaches zero while the higher energies increase as strength of the field $B_{x0} = B_{y0}$ are increased past 2Δ .

The form of the phase diagram shown in Fig. 3 makes it clear that the robustness of the MBS to eccentricity of the magnetic field helicity depends strongly on the magnitude of the larger field component; in fact, the topological phase could be reached even when one of the magnetic field components is much smaller than the other, provided that the larger component is near 2Δ . To explore this region of the phase diagram in more detail, we plot the two lowest energy states, E_0 and E_1 as a function of one component of the magnetic field, B_{x0} or B_{y0} , while keeping the other component equal to zero, see Fig. 4(b). We observe that the lowest energy E_0 reaches its minimum when the non-zero component is $\approx 2\Delta$ and then increases as the field component is increased further. We note that in these plots, for which one component of the field is zero, there is no topologically protected phase.

Figure 4(c) shows the energies of the two lowest-energy excitations, $E_{0,1}$ as function of the magnetic field strength of one component, while the other is fixed at 2Δ . We notice that for both $B_{x0} = 2\Delta$ (solid lines) or $B_{y0} = 2\Delta$ (dashed lines), the lowest energy excitation vanishes quickly as the magnitude of the other field component is increased.

While the actual orientation of magnetic field components B_{x0} and B_{y0} is arbitrary with respect to the direction of the wire, the dependence of the energies on the two components are not identical since the field magnitude at the ends of the wire is determined by the value of B_{x0} , while the B_y field always vanishes at the wire ends, see Eq. (5). This distinction between components explains a weak asymmetry of the phase diagram with respect to line $B_{x0} = B_{y0}$ in Fig. 3. The distinction is even more pronounced in the energy plots shown Figs. 4(b) and 4(c). When $B_{x0} = 0$ and $B_{y0} \neq 0$, the low energy levels, such as $E_{0,1}$, are doubly degenerate. In the opposite case, $B_{x0} \neq 0$ and $B_{y0} = 0$, this double degeneracy is split, pushing the lowest energy closer to zero, see the lowest solid line in Fig. 4(b). The double degeneracy is always split by $B_{x0} \neq 0$, as shown by the lower two dashed lines in Fig. 4(c).

Overall, the above analysis demonstrates that the topological phase with MBS is possible when the dominant magnetic field has magnitude about 2Δ and the minor component is strong enough to open the gap in the energy spectrum and push the energy of the MBS to zero. MBS are enhanced further when the dominant field component is at its maximum value at the wire ends.

C. Localization length

The coherence length is important energy scale of a superconductor and is inversely proportional to the superconducting energy gap:

$$\xi = \frac{\hbar v_F}{E_1}. \quad (27)$$

Equation (27) takes into account that in the topological superconducting phase, the lowest energy state corresponds to the MBS and the superconducting gap is determined by the next positive energy E_1 . In this subsection we argue that the localization length ζ of the MBS near the wire ends is consistent with the correlation length determined by Eq. (27), $\zeta \simeq \xi$. We also show that the lowest positive energy E_0 agrees well with the exponential dependence on wire length L as $E_0 \propto \exp(-L/\xi)$. The behavior of the localization length for helical fields with elliptical cross-section is qualitatively similar to that found for purely helical fields.

Figure 5(a) shows on a semilog scale the lowest energy as a function of $B_{x0} = B_{y0}$, corresponding to a perfectly helical field.⁵³ For $B_{x0} = B_{y0} = B_0 > \Delta$ the lowest excitation eigenenergy $E_0 > 0$ decreases exponentially with B_0 , as demonstrated in Fig. 5(a). To demonstrate the dependence on wire length, we show the energy versus B_0 for wires with length $L = 20$ (solid line), $L = 40$, (dashed line) and $L = 80 \mu\text{m}$ (dash-dotted line) and compare the result with exponential fit $\propto \exp(-L/\xi)$, where ξ is evaluated from Eq. (27) with numerical values of E_1 (E_1 is presented in Fig. 4(a) for $L = 40$ and $80 \mu\text{m}$.)

Figure 5(b) examines the case of an elliptical helical field; it is a semilog plot of the three lowest excitation energies as a function of one field component (either B_{x0} or B_{y0}) as the other is held fixed at 2Δ . As the variable magnetic field component is increased from zero, the lowest energy E_0 decreases towards zero. The lowest energy E_0 again decreases exponentially with the wire length L as $\propto \exp(-L/\xi)$ with ξ evaluated from Eq. (27) with E_1 shown in Fig. 4(c) by a dashed line for $B_{x0} = 2\Delta$ and variable B_{y0} .

We also calculate the localization length by examining the wavefunction of the lowest energy excitation (the eigenvector with energy eigenvalue E_0). To characterize the localization length, we define the following integral expression that effectively evaluates the distance of the ‘center-of-mass’ of the MBS wave function from the wire ends:

$$\zeta = 2\delta r \left(\sum_{n=0}^{N/2} n P_n + \sum_{n=N/2}^N (N-n) P_n \right), \quad (28)$$

where P_n is the probability density for the MBS at site n :

$$P_n = \Phi_n^\dagger \Phi_n, \quad \Phi_n = \Phi(n\delta r), \quad (29)$$

and $\Phi(\mathbf{r})$ is obtained from the state $\Psi(\mathbf{r})$ corresponding to the lowest positive eigenenergy of Eq. (9) via transformation (10).

The dependence of the localization length ζ on the magnetic field is shown in Fig. 5(c) a perfect helical field as

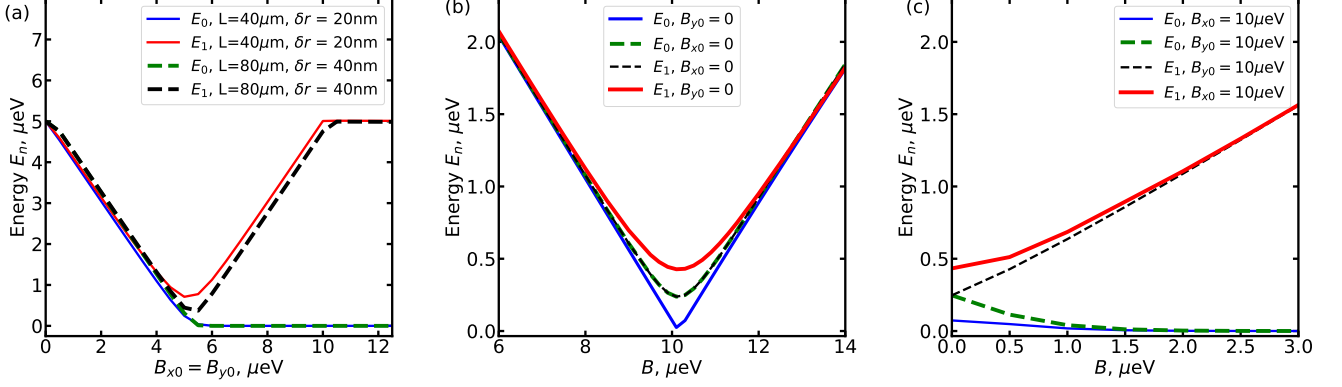


FIG. 4. Comparison of two lowest-energy excitation energies E_0 and E_1 in non-topological and topological phases as a function of magnetic field magnitude. (a): Energies E_0 and E_1 versus the magnetic field amplitude $B_{x0} = B_{y0}$ in wires evaluated for different wire lengths, solid lines: $L = 40 \mu\text{m}$ and $\delta r = 20\text{nm}$; dashed lines: $L = 80 \mu\text{m}$ and $\delta r = 40\text{nm}$. In the topologically nontrivial phase, E_0 approaches zero for when $B_{x0} = B_{y0}$ is large. The second excitation energy E_1 reaches its minimum at the phase transition, where the gap in the density of states closes in the infinitely long wire, and then increases as the magnetic field is increased further. (b): Energies of the lowest two excitations as a function of one component of the field, $B_{x0} = B$ (solid lines) or $B_{y0} = B$ (dashed lines), while the other component is strictly zero, $B_{y0} = 0$ or $B_{x0} = 0$, respectively. When one field component is zero, the magnetic field has no helicity and no topologically protected state can form. All the excitation energies show minima at $B \simeq 2\Delta = 10 \mu\text{eV}$ and then all energies increase as B is increased further. When $B_{x0} = 0$ and the magnetic field is zero at the ends of the wire, $E_0 = E_1$, but the energies E_0 and E_1 are split near $B_{x0} = 2\Delta$ when the field at the ends is not zero ($B_{y0} = 0$ case). (c): Energies of the lowest energy excitations as a function of one component of the magnetic field when the other component is fixed at twice the superconducting gap Δ , either $B_{x0} = B$, $B_{y0} = 2\Delta$ or $B_{y0} = B$, $B_{x0} = 2\Delta$. For both cases, the energy of the lowest-energy state monotonically decreases towards zero as B increases, while all other excitation energies increase as the superconducting gap opens, consistent with a topologically nontrivial phase. For all these plots, the proximity-induced superconducting order parameter $\Delta = 5 \mu\text{eV}$, and the chemical potential $\mu = \hbar^2 Q^2 / 8m = 49.6 \mu\text{eV}$ is matched to the middle of the magnetic superlattice gap. For panels (b) and (c), the wire length is $L = 40 \mu\text{m}$.

a function of field magnitude and in Fig. 5(d) for the case where one field component is fixed at 2Δ and the magnitude of the other component is varied. We calculate the localization length using Eq. (28) for several values of the nanowire length. At $B_{x0} = B_{y0} < \Delta$, evaluated values of the localization length ζ is comparable to the length of the wire. At larger fields, ζ decreases rapidly and reaches the value $\zeta \simeq \xi/2$, where $\xi_{\text{sc}} = \hbar^2 Q / (2m\Delta) \simeq 1.26 \mu\text{m}$ the superconducting coherence length that determines $|\Psi_n|^2 \propto \exp(-2n\delta r/\xi)$. Figs. 5(c) and 5(d) also show that the estimate of the localization length using the dependence of the coherence length ξ on E_1 agrees well with the estimate of the MBS localization length done using Eq. (28).

D. Dependence of the phase diagram on chemical potential

We now investigate the phase diagram when the chemical potential μ is not located in the middle of energy spectrum gap of magnetic superlattice, so that $\mu = \hbar^2 Q^2 / 8m + \delta\mu$ with $\delta\mu \neq 0$.

It is straightforward to extend the analytic theory developed in Sec. III to the case in which $\delta\mu \neq 0$. The excitation energies of Hamiltonian (15) are

$$E_{\theta}^{\pm} = \sqrt{B_{\theta}^2 + \Delta^2 + \delta\mu^2 + v_F^2 \delta k^2} \pm 2D, \quad (30)$$

with

$$D = \sqrt{B_{\theta}^2 (\Delta^2 + \delta\mu^2) + \delta\mu^2 v_F^2 \delta k^2}. \quad (31)$$

The lowest energy for real δk is achieved for $\delta k = 0$ and is given by

$$E_{\theta}^{-} = |B_{\theta} - \sqrt{\Delta^2 + \delta\mu^2}|, \quad (32)$$

and the gap closes for $B_{\theta} = \sqrt{\Delta^2 + \delta\mu^2}$. This expression is similar to the condition for the point of the phase transition in perfect helical magnetic field^{31,32}. For fixed Δ and $\delta\mu$, the gap closes when

$$B_{+} = (B_{x0} + B_{y0})/2 > \sqrt{\Delta^2 + \delta\mu^2}. \quad (33a)$$

This condition specifies the magnitude of the magnetic field necessary to develop the topologically nontrivial superconducting phase.^{11,12,16} The second condition for the topological phase is determined by ellipticity of the spiral magnetic field that limits the relative mismatch between B_{x0} and B_{y0} components. At non-zero $\delta\mu$, the corresponding condition is

$$|B_{-}| < \sqrt{\Delta^2 + \delta\mu^2}, \quad (33b)$$

with $B_{-} = (B_{x0} - B_{y0})/2$. We notice that Eq. (33b) implies that non-zero $\delta\mu$ makes the system more robust to imperfect helical magnetic fields, but at the same time, Eq. (33a)

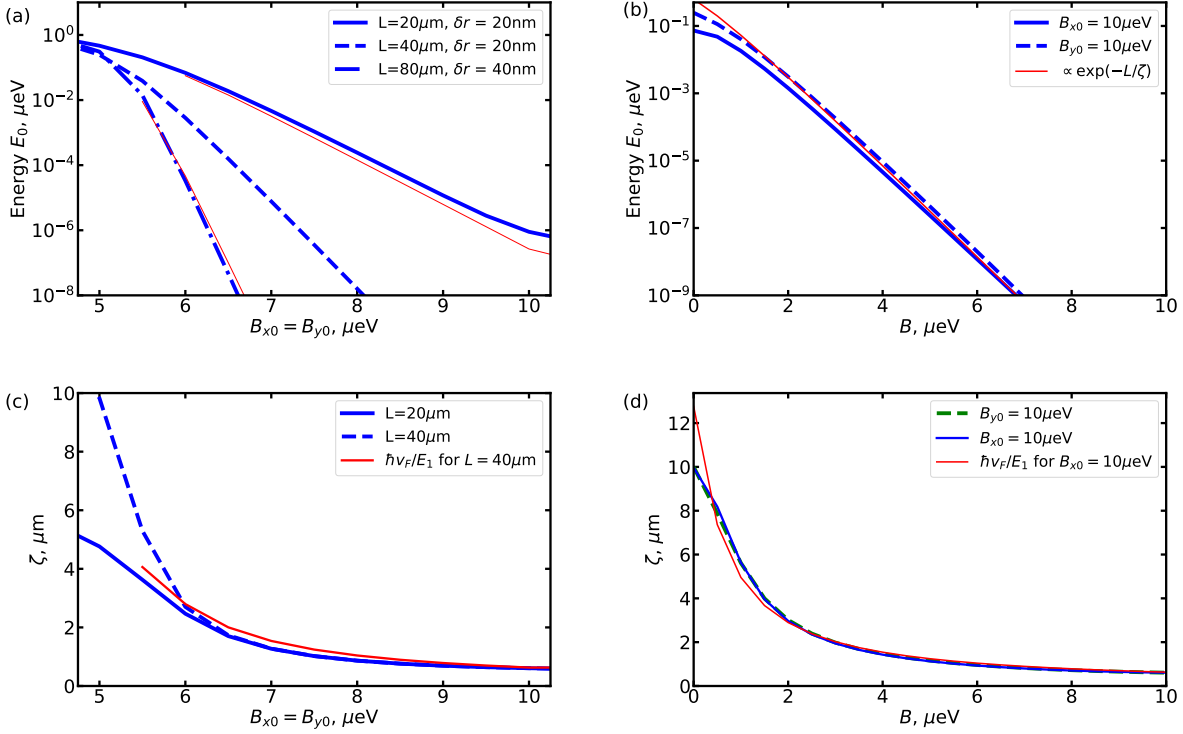


FIG. 5. (a): Numerically obtained value of the lowest positive energy E_0 as function of the magnetic field amplitude $B_{x_0} = B_{y_0}$ in wires of length $L = 20\mu\text{m}$ (solid line) and $L = 40\mu\text{m}$ (dashed line) obtained using $\delta r = 20\text{nm}$ and $L = 80\mu\text{m}$ obtained using $\delta r = 40\text{nm}$. The onset of exponential decrease of E_0 with increasing $B_{x_0} = B_{y_0}$ above Δ indicates the transition to the topologically nontrivial superconducting phase, with the stronger dependence in longer wires arising because the overlap between MBS decreases exponentially with wire length. Thin red lines show $E \propto \exp(-L/\xi)$, where ξ is given by Eq. 27. (b): Numerically obtained value of the lowest positive energy E_0 in wires of length $L = 40\mu\text{m}$ as function of the magnetic field amplitude B_{y_0} (solid line) or B_{x_0} (dashed line) fixed with $B_{x_0} = 2\Delta$ or $B_{y_0} = 2\Delta$, respectively. The similarity of the behavior to that seen in (a) demonstrates the robustness of the topologically nontrivial phase to ellipticity in the helical magnetic field. Energy E_0 decreases exponentially as L/ξ is increased, as demonstrated by thin red line for $\propto \exp(-L/\xi)$, where ξ is computed from Eq. (27) using $E_1(B_{y_0})$ at $B_{x_0} = 2\Delta$, see red solid line in Fig. 4(c). (c): Numerical obtained localization length of the lowest-energy state ζ , obtained using Eq. (28) versus the strength of the magnetic field for a perfect helix, $B_{x_0} = B_{y_0}$, in wires of length $L = 20\mu\text{m}$ (solid line), $40\mu\text{m}$ (dashed line). Also shown as the thin red line is the localization length ξ , Eq. (27), obtained using values of E_1 for a wire of length $L = 40\mu\text{m}$, see red solid line in Fig. 4(a). (d): Numerically obtained localization lengths of the lowest-energy state, obtained using Eq. (28) versus the magnitude of B_{x_0} (dashed line) or B_{y_0} (solid line) with $B_{y_0} = 2\Delta$ or $B_{x_0} = 2\Delta$, respectively, in wires of length $L = 40\mu\text{m}$. Also shown as the thin red line is the localization length ξ obtained from Eq. (27) using $E_1(B_{x_0} = 2\Delta, B_{y_0} = B)$ as function of B , see solid red line in Fig. 4(b). The similarity to (c) demonstrates the robustness of the topological phase to ellipticity in the helical magnetic field. In all panels, superconducting gap parameter $\Delta = 5\mu\text{eV}$ and chemical potential $\mu = \hbar^2 Q^2/8m = 49.6\mu\text{eV}$, which is matched to the middle of the magnetic superlattice gap.

implies that stronger fields are needed to reach the topologically nontrivial phase. The conditions for the existence of the MBS at $\delta\mu = 0$ can be interpreted as requiring that one out of the two electron bands has a gap in the energy interval $\hbar^2 Q^2/8m \pm \Delta$ while the other does not. When $\delta\mu \neq 0$, we find that a similar condition applies. If at the Fermi momentum one of the bands is gapped while the other is not, then a topologically nontrivial phase can be supported. The mismatch of the Fermi momentum with the points of 1D Brillouin zone correspond to the superconducting excitation with energy $\hbar^2 Q^2/8m \pm \sqrt{\Delta^2 + \delta\mu^2}$, and the MBS exists if these energies cross one and only one band of electrons in the magnetic superlattice, see Fig. 2.

We also performed numerical investigations of systems

with $\delta\mu \neq 0$ for wires of finite length. Figure 6 shows the results for a phase diagram obtained for a wire with length $L = 20\mu\text{m}$ by showing the energy of the lowest-energy state as a function of the magnitudes of the magnetic field components. We define the regions of field in which the system is in a topologically nontrivial phase and MBS are supported to be those where the lowest-energy state has energy that is much less than that of the superconducting gap. A comparison of the results in Fig. 6 with those in Fig. 3 demonstrate that tuning the chemical potential of the nanowire can play an important role in optimizing the robustness of MBS.

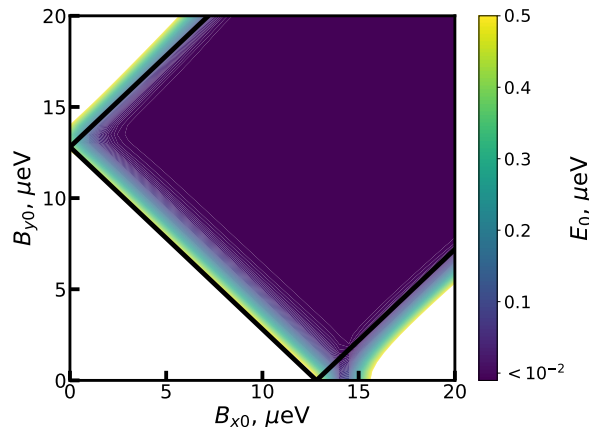


FIG. 6. Contour plot of the lowest positive energy E_0 of the system in the plane of magnetic field amplitudes B_{x0} and B_{y0} for the chemical potential $\mu = \hbar^2 Q^2 / 8m + \delta\mu$ with $\delta\mu = 4 \mu\text{eV}$. Here, the superconducting pairing energy $\Delta = 5 \mu\text{eV}$, and the wire length $L = 20 \mu\text{m}$. The region with energy E_0 above $0.5 \mu\text{eV}$ corresponds to the gapped non-topological superconducting phase and is shown as unfilled parts of the B_{x0} - B_{y0} plane. The solid straight lines represent the analytical expressions (33) for the phase boundaries derived for linearized bands and an infinite length wire. In wires of finite length, the zero energy state develops over finite crossover region shown as transition colors in the color plot for the region of $E_0 < 0.5 \mu\text{eV}$, the dark purple color shows area where E_0 drops below $10^{-2} \mu\text{eV}$.

V. CONCLUSIONS

Motivated by the possibility of introducing strong artificial spin-orbit coupling in nanowires fabricated in silicon, we have considered a nanowire-superconductor hybrid structure with a non-uniform magnetic field and studied the conditions for which the superconductivity is topologically nontrivial and MBS appear. We have investigated both analytically and numerically the case of a spiral magnetic field with an elliptical cross-section, which becomes helical for a round cross-section. This spatial dependence is similar to the magnetic field configurations obtained in Ref. 44, which were achieved

using nanomagnet arrays compatible with current lithographic techniques. Here, we have shown that this system can support MBS even when the magnitudes of the two components of the helical field are substantially different.

The robustness of topological superconductivity to ellipticity of the helical magnetic field depends strongly on the magnitude of the dominant field component. If the magnitude of this component is optimized, by making its value twice the superconducting pairing energy Δ , then a topological phase appears, even when the other magnetic field component is small. Analytic theory for an infinite length wire with a linearized electronic spectrum provides an excellent guide for interpreting results obtained numerically for a discretized model using finite-length wires.

We have also investigated the localization length of the MBS. The dependence of the energy on wire length, for the lowest energy excitation, is consistent with a simple picture in which the energy is proportional to the overlap of two exponentially localized states at the ends of the wire.

Our results provide evidence that using lithographically patterned micromagnets is a viable method for creating spatially-dependent magnetic fields that, together with proximity-induced superconductivity, can be used to generate MBS. Because intrinsic spin-orbit coupling is not required, many materials systems could also be suitable hosts for MBS, in addition to the silicon wires considered here.

ACKNOWLEDGMENTS

We thank Anton Akhmerov, Ryan Foote, Alex Levchenko, Constantin Schrader, Brandur Thorgrímsson, and Hongyi Xi for helpful discussions. This work was supported by the Vannevar Bush Faculty Fellowship program sponsored by the Basic Research Office of the Assistant Secretary of Defense for Research and Engineering and funded by the Office of Naval Research through Grant No. N00014-15-1-0029, by NSF EA-GER Grant No. DMR-1743986, by the Army Research Office, Laboratories for Physical Sciences Grant No. W911NF-18-1-0115. The views and conclusions contained here are those of the authors and should not be interpreted as representing the official policies, either expressed or implied, of the Office of Naval Research or the U.S. Government.

¹ C. Nayak, S. H. Simon, A. Stern, M. Freedman, S. Das Sarma, *Rev. Mod. Phys.* **80**, 1083 (2008).
² J. Alicea, *Rep. Prog. Phys.* **75**, 076501 (2012).
³ A. Y. Kitaev, *Phys. Usp.* **44**, 131 (2001).
⁴ L. Fu and C. L. Kane, *Phys. Rev. Lett.* **100**, 096407 (2008).
⁵ Y. Tanaka, T. Yokoyama, and N. Nagaosa, *Phys. Rev. Lett.* **103**, 107002 (2009).
⁶ F. Wilczek, *Nature Phys.* **5**, 614 (2009).
⁷ A. R. Akhmerov, J. Nilsson, and C. W. J. Beenakker, *Phys. Rev. Lett.* **102**, 216404 (2009).
⁸ M. Franz, *Physics* **3**, 24 (2010).

⁹ A. Stern, *Nature (London)* **464**, 187 (2010).
¹⁰ J. D. Sau, R. M. Lutchyn, S. Tewari, and S. Das Sarma, *Phys. Rev. Lett.* **104**, 040502 (2010).
¹¹ R. M. Lutchyn, J. D. Sau, and S. Das Sarma, *Phys. Rev. Lett.* **105**, 077001 (2010).
¹² Y. Oreg, G. Refael, and F. von Oppen, *Phys. Rev. Lett.* **105**, 177002 (2010).
¹³ J. Alicea, *Phys. Rev. B* **81**, 125318 (2010).
¹⁴ K. Flensberg, *Phys. Rev. B* **82**, 180516 (2010).
¹⁵ M. Duckheim and P. W. Brouwer, *Phys. Rev. B* **83**, 054513 (2011).
¹⁶ J. Klinovaja, P. Stano, and D. Loss, *Phys. Rev. Lett.* **109**, 236801 (2012).

- (2012).
- ¹⁷ M. Kjaergaard, K. Wölms, and K. Flensberg, *Phys. Rev. B* **85**, 020503(R) (2012).
 - ¹⁸ S. Turcotte, S. Boutin, J. C. Lemyre, I. Garate, and M. Pioro-Ladrière, arXiv:1904.06275 (2019).
 - ¹⁹ V. Mourik, K. Zuo, S. M. Frolov, S. R. Plissard, E. P. A. M. Bakkers, and L. P. Kouwenhoven, *Science* **336**, 1003 (2012).
 - ²⁰ M. T. Deng, C. L. Yu, G. Y. Huang, M. Larsson, P. Caroff, and H. Q. Xu, *Nano Lett.* **12**, 6414 (2012).
 - ²¹ A. Das, Y. Ronen, Y. Most, Y. Oreg, M. Heiblum, and H. Shtrikman, *Nature Phys.* **8**, 887 (2012).
 - ²² L. P. Rokhinson, X. Liu, and J. K. Furdyna, *Nat. Phys.* **8**, 795 (2012).
 - ²³ A. D. K. Finck, D. J. Van Harlingen, P. K. Mohseni, K. Jung, and X. Li, *Phys. Rev. Lett.* **110**, 126406 (2013).
 - ²⁴ H. O. H. Churchill, V. Fatemi, K. Grove-Rasmussen, M. T. Deng, P. Caroff, H. Q. Xu, and C. M. Marcus, *Phys. Rev. B* **87**, 241401(R) (2013).
 - ²⁵ S. Nadj-Perge, I. K. Drozdov, J. Li, H. Chen, S. Jeon, J. Seo, A. H. MacDonald, B. A. Bernevig, A. Yazdani, *Science* **346**, 602 (2014).
 - ²⁶ A. P. Higginbotham, S. M. Albrecht, G. Kiršanskas, W. Chang, F. Kuemmeth, P. Krogstrup, T. S. Jespersen, J. Nygård, K. Flensberg, and C. M. Marcus, *Nature Phys.* **11**, 1017 (2015).
 - ²⁷ S. M. Albrecht, A. P. Higginbotham, M. Madsen, F. Kuemmeth, T. S. Jespersen, J. Nygård, P. Krogstrup, and C. M. Marcus, *Nature* **531**, 206 (2016).
 - ²⁸ M. T. Deng, S. Vaitiekėnas, E. B. Hansen, J. Danon, M. Leijnse, K. Flensberg, J. Nygård, P. Krogstrup, and C. M. Marcus, *Science* **354**, 1557 (2016).
 - ²⁹ H. Zhang, Ö. Gül, S. Conesa-Boj, M. P. Nowak, M. Wimmer, K. Zuo, V. Mourik, F. K. de Vries, J. van Veen, M. W. A. de Moor, J. D. S. Bommer, D. J. van Woerkom, D. Car, S. R. Plissard, E. P. A. M. Bakkers, M. Quintero-Pérez, M. C. Cassidy, S. Koelling, S. Goswami, K. Watanabe, T. Taniguchi, and L. P. Kouwenhoven, *Nat. Commun.* **8**, 16025 (2017).
 - ³⁰ H. Zhang, C.-X. Liu, S. Gazibegovic, D. Xu, J. A. Logan, G. Wang, N. van Loo, J. D. S. Bommer, M. W. A. de Moor, D. Car, R. L. M. Op het Veld, P. J. van Veldhoven, S. Koelling, M. A. Verheijen, M. Pendharkar, D. J. Pennachio, B. Shojaei, J. S. Lee, C. J. Palmstrøm, E. P. A. M. Bakkers, S. Das Sarma, and L. P. Kouwenhoven, *Nature* **556**, 74 (2018).
 - ³¹ B. Braunecker, G. I. Japaridze, J. Klinovaja, and D. Loss, *Phys. Rev. B* **82**, 045127 (2010).
 - ³² R. Egger and K. Flensberg, *Phys. Rev. B* **85**, 235462 (2012).
 - ³³ T.-P. Choy, J. M. Edge, A. R. Akhmerov, and C. W. J. Beenakker, *Phys. Rev. B* **84**, 195442 (2011).
 - ³⁴ M. M. Vazifeh and M. Franz, *Phys. Rev. Lett.* **111**, 206802 (2013).
 - ³⁵ B. Braunecker and P. Simon, *Phys. Rev. Lett.* **111**, 147202 (2013).
 - ³⁶ S. Nadj-Perge, I. K. Drozdov, B. A. Bernevig, and A. Yazdani, *Phys. Rev. B* **88**, 020407(R) (2013).
 - ³⁷ F. Pientka, L. I. Glazman, and F. von Oppen, *Phys. Rev. B* **88**, 155420 (2013).
 - ³⁸ M. Ruby, F. Pientka, Y. Peng, F. von Oppen, B. W. Heinrich, and K. J. Franke, *Phys. Rev. Lett.* **115**, 197204 (2015).
 - ³⁹ G. L. Fatin, A. Matos-Abiague, B. Scharf, and I. Žutić, *Phys. Rev. Lett.* **117**, 077002 (2016).
 - ⁴⁰ A. Matos-Abiague, J. Shabani, A. D. Kent, G. L. Fatin, B. Scharf, and I. Žutić, *Solid State Commun.* **262**, 1 (2017).
 - ⁴¹ T. Ojanen, *Phys. Rev. B* **88**, 220502(R) (2013).
 - ⁴² N. Sedlmayr, J. M. Aguiar-Hualde, and C. Bena, *Phys. Rev. B* **91**, 115415 (2015).
 - ⁴³ S. Boutin, J. C. Lemyre, and I. Garate, *Phys. Rev. B* **98**, 214512 (2018).
 - ⁴⁴ L. N. Maurer, J. K. Gamble, L. Tracy, S. Eley, and T. M. Lu, *Phys. Rev. Applied* **10**, 054071 (2018).
 - ⁴⁵ Krogstrup P, Ziino NLB, Chang W, Albrecht SM, Madsen MH, Johnson E et al. Epitaxy of semiconductor superconductor nanowires. *Nat Mater* 2015; 14: 400406.
 - ⁴⁶ E. Bustarret, C. Marcenat, P. Achatz, J. Kačmarčík, F. Lévy, A. Huxley, L. Ortéga, E. Bourgeois, X. Blase, D. Débarre, and J. Boulmer, *Nature* **444**, 465 (2006).
 - ⁴⁷ M. Friesen, S. Chutia, C. Tahan, and S. N. Coppersmith, *Phys. Rev. B* **75**, 115318 (2007).
 - ⁴⁸ J. K. Gamble et al., *Appl. Phys. Lett.* **109**, 253101 (2016).
 - ⁴⁹ D. J. Ibberson, L. Bourdet, J. C. Abadillo-Uriel, I. Ahmed, S. Barraud, M. J. Calderón, Y.-M. Niquet, and M. F. Gonzalez-Zalba, *Appl. Phys. Lett.* **113**, 053104 (2018).
 - ⁵⁰ D. Laroche, S.-H. Huang, E. Nielsen, Y. Chuang, J.-Y. Li, C. W. Liu, and T. M. Lu, *AIP Advances* **5**, 107106 (2015).
 - ⁵¹ N. W. Ashcroft and N. D. Mermin, *Solid State Physics*, Brooks/Cole, Pacific Grove, CA (1976)
 - ⁵² P.G. de Gennes, *Superconductivity of Metals and Alloys* (WA Benjamin, New York, 1966), Vol. 86.
 - ⁵³ J. Klinovaja and D. Loss, *Phys. Rev. B* **86**, 085408 (2012).